A numerical study of three-dimensional turbulent channel flow at large Reynolds numbers

By JAMES W. DEARDORFF

National Center for Atmospheric Research, Boulder, Colorado 80302

The three-dimensional, primitive equations of motion have been integrated numerically in time for the case of turbulent, plane Poiseuille flow at very large Reynolds numbers. A total of 6720 uniform grid intervals were used, with sub-grid scale effects simulated with eddy coefficients proportional to the local velocity deformation. The agreement of calculated statistics against those measured by Laufer ranges from good to marginal. The eddy shapes are examined, and only the u-component, longitudinal eddies are found to be elongated in the downstream direction. However, the lateral v eddies have distinct downstream tilts. The turbulence energy balance is examined, including the separate effects of vertical diffusion of pressure and local kinetic energy.

It is concluded that the numerical approach to the problem of turbulence at large Reynolds numbers is already profitable, with increased accuracy to be expected with modest increase of numerical resolution.

1. Introduction

For better understanding of turbulent flow, numerical integration in time and in three-dimensional space has several promising and distinguishing aspects. First, a detailed integration allows examination of flow patterns which produce the turbulence statistics, after sufficient time has elapsed since initial conditions were imposed. Phase information is retained so that typical flow structures including tilts and elongations of eddies may be studied. Secondly, except for effects of motions on scales too small and too large to resolve, the calculated motions are treated rigorously. The assumptions which are required because of the two scale effects become less crucial as computer speed and storage capacity increase. Third, these assumptions can be expressed very simply thereby enabling a large number of investigators to understand them and to introduce their own improvements. Finally, complications such as those introduced by unusual boundary conditions or by the presence of additional forces are easily incorporated into the numerical model.

Numerical methods for use in three dimensions have been reported by Harlow & Welch (1965), Aziz & Hellums (1967), Orszag (1969) and Chorin (1968). However, they treated motions with scales ranging down to the viscous cut-off and were therefore limited to relatively weak flows and small Reynolds numbers or Rayleigh numbers. The numerical resolution of all relevant scales for large

Printed in Great Britain

Reynolds numbers was first emphasized to be impossible by Corrsin (1961) and appears to be almost as impossible today.

The idea of applying an averaging operator to the governing equations, with averaging typically being over the grid volume of the calculations to filter out the subgrid scale (SGS) motions, has been known since the early work of Reynolds (1895). Explicit calculations can then be made for the filtered variables after assumptions are made for the SGS Reynolds stresses which arise from the averaging process. This approach has been employed by several groups of meteorologists (Smagorinsky, Manabe & Halloway 1965; Leith 1965; Mintz 1965; Kasahara & Washington 1967) for the general circulation of the atmosphere with considerable success. Although their calculated flows are somewhat two-dimensional in that vertical accelerations are neglected and vertical velocities turn out to be very small in comparison with horizontal velocities, there is no reason why their general approach cannot be used successfully also in the study of fully three-dimensional turbulence.

Furthermore, considerable research has already been carried out by Smagorinsky *et al.* (1965) and Lilly (1967) on an assumption which can be made for the SGS Reynolds stresses and which may be applicable if an inertial subrange exists on scales encompassing the grid interval. The assumption, to be discussed in § 3, is applicable only for large Reynolds numbers.

The main purpose of the paper is to test this meteorological approach upon an interesting case of laboratory turbulence: plane Poiseuille flow (channel flow) driven by a uniform pressure gradient. To the extent that the numerical results may be trusted, a second purpose is to examine properties of the turbulence patterns and statistics some of which cannot be measured experimentally.

2. Governing equations with grid-scale averaging

Following Reynolds (1895), let the grid-scale averaging operator acting upon some dependent variable $u(x, y, z, t)$ be defined by the overbar symbol (¯) as follows:

$$\bar{u}(x, y, z, t) = \frac{1}{\Delta x \cdot \Delta y \cdot \Delta z} \int_{x-\frac{1}{2}\Delta x}^{x+\frac{1}{2}\Delta x} \int_{y-\frac{1}{2}\Delta y}^{y+\frac{1}{2}\Delta y} \int_{z-\frac{1}{2}\Delta z}^{z+\frac{1}{2}\Delta z} u(\xi, \eta, \zeta, t) \, d\zeta \, d\eta \, d\xi, \qquad (2.1)$$

where ξ, η, and ζ are dummy variables representing x, y, and z, respectively, and Δx, Δy, and Δz are the corresponding grid increments of the finite-difference equations. A filtered variable, denoted by the overbar, is thus a continuous function of space and time. Its spatial derivatives in finite-difference form should not be subject to excessive truncation errors because SGS components are almost entirely filtered out. Time derivatives in finite-difference form likewise will not have excessive truncation errors if the time increment Δt is sufficiently small as, for example, is required by certain explicit numerical stability criteria.

After applying the overbar operator, the Navier–Stokes equations in flux form may be written

$$\frac{\partial \bar{u}_i}{\partial t} = -\frac{\partial}{\partial x_j}\left[\bar{u}_i\bar{u}_j + \overline{u_i'u_j'} - \tfrac{1}{3}\delta_{ij}\overline{u_l'u_l'}\right] - \frac{\partial}{\partial x_i}\left[\frac{\bar{p}}{\rho_0 u^{*2}} + \tfrac{1}{3}\overline{u_l'u_l'}\right] - \delta_{i3}\frac{gh}{u^{*2}} + R^{-1}\nabla^2\bar{u}_i. \quad (2.2)$$

Here $i, j = 1, 2, 3$ correspond to x, y, z, respectively, where x is in the downstream direction, y is in the *lateral* direction parallel to the boundaries, and z is in the direction normal to the boundaries, here taken to be vertical.

All velocities and co-ordinates in (2.2) have been made dimensionless by means of the length scale h separating the parallel boundaries, by the friction velocity $u^* = (\tau/\rho_0)^{\frac{1}{2}}$, and by the time scale h/u^*. The quantity τ is the wall stress; ρ_0 the density which is assumed constant; $\bar{p}/\rho_0 u^{*2}$ the dimensionless, resolvable pressure; g the gravitational acceleration; R the Reynolds number u^*h/ν; and ν the kinematic viscosity.

The primes are deviations from local grid-volume means, and the term $\overline{u_i' u_j'}$ thus represents the subgrid scale (SGS) Reynolds stress tensor. Reynolds' averaging assumption

$$\overline{\overline{u_i}\,\overline{u_j}} - \overline{u}_i\,\overline{u}_j + \overline{\overline{u}_i\,u_j'} + \overline{u_i'\,\overline{u}_j} = 0$$

has been applied in expressing $\overline{u_i u_j}$ as $\overline{u}_i \overline{u}_j + \overline{u_i' u_j'}$. However, this assumption is not separately necessary and may be incorporated into later assumptions if $\overline{u_i' u_j'}$ is formally replaced by $\overline{u_i u_j} - \overline{u}_i \overline{u}_j$ wherever it appears (see Lilly 1967).

For a reason to be apparent in § 3, $\frac{1}{3}\overline{u_l' u_l'}$ has been added to $\bar{p}/\rho_0 u_*^2$ and subtracted from the Reynolds-stress terms. (The summation convention is used here.)

Now, denote the horizontal average of a quantity by the angular brackets: $\langle\ \rangle$. The horizontal average of the continuity equation

$$\frac{\partial \overline{u}_i}{\partial x_i} = 0 \tag{2.3}$$

for fully developed flow between parallel boundaries at $z = 0$, 1 then requires $\langle \overline{w} \rangle = 0$ and $\langle \partial \overline{w}/\partial t \rangle = 0$. To ensure this condition when the pressure is not obtained exactly, the horizontal average of (2.2) for $i = 3$ may be subtracted from (2.2) to give

$$\frac{\partial \overline{u}_i}{\partial t} = -\frac{\partial}{\partial x_j}\left[\overline{u}_i \overline{u}_j + \overline{u_i' u_j'} - \tfrac{1}{3}\delta_{ij}\,\overline{u_l' u_l'} - \delta_{i3}\,\delta_{j3}\langle \overline{u_3^2} + \overline{u_3'^2} - \tfrac{1}{3}\overline{u_l' u_l'}\rangle\right]$$

$$-\frac{\partial}{\partial x_i}(\overline{P}'' - 2x_1) + R^{-1}\nabla^2 \overline{u}_i, \tag{2.4}$$

where
$$\overline{P}'' = (\overline{p}/\rho_0 u^{*2} + \tfrac{1}{3}\overline{u_l' u_l'} + 2x_1) - \langle \overline{p}/\rho_0 u^{*2} + \tfrac{1}{3}\overline{u_l' u_l'} + 2x_1\rangle \tag{2.5}$$

and the double prime ( )″ denotes the deviation of a quantity from the horizontal average. Then it identically follows upon application of horizontal averaging to (2.4) that the right-hand side vanishes for $i = 3$.

The quantity $(\partial/\partial x_i)\,2x_1$ ($= 2$ when $i = 1$) in (2.4) is the dimensionless, gross downstream pressure gradient which would maintain a steady flow against the equilibrium, long-term wall friction u^{*2}, produced by both boundaries. For purposes of visual examination of pressure eddies, it is convenient to remove this trend from $\overline{p}/\rho_0 u^{*2}$.

In this study, the Reynolds number will be considered very large so that the viscous term can be neglected. The viscous sublayer at the walls will therefore

not be treated explicitly. Equation (2.4) then can be written

$$\frac{\partial \overline{u}_i}{\partial t} = \overline{Q}_i - \frac{\partial}{\partial x_i}(\overline{P}'' - 2x_1), \tag{2.6a}$$

where
$$\overline{Q}_i = -\frac{\partial}{\partial x_j}[\overline{u}_i \overline{u}_j + \overline{u'_i u'_j} - \tfrac{1}{3}\delta_{ij}\overline{u'_l u'_l} - \delta_{i3}\delta_{j3}\langle\overline{u_3^2} + \overline{u'_3{}^2} - \tfrac{1}{3}\overline{u'_l u'_l}\rangle]. \tag{2.6b}$$

From (2.6a, b) the Poisson equation from which $\overline{P}''$ is to be calculated is

$$\nabla^2 \overline{P}'' = \frac{\partial \overline{Q}_i}{\partial x_i} - \frac{\partial}{\partial t}\left(\frac{\partial \overline{u}_i}{\partial x_i}\right), \tag{2.7}$$

where ∇^2 is the Laplacian operator in three dimensions. Although the last term in (2.7) vanishes because of (2.3), it is retained here in anticipation of §5.

3. Representation of subgrid scale (SGS) Reynolds stresses

Remaining as unknowns in (2.4) are the SGS Reynolds stresses $\overline{u'_i u'_j} - \tfrac{1}{3}\delta_{ij}\overline{u'_l u'_l}$. The method of evaluation used here introduces SGS eddy coefficients in partial analogy to the molecular case:

$$\overline{u'_i u'_j} - \tfrac{1}{3}\delta_{ij}\overline{u'_l u'_l} = -K\left(\frac{\partial \overline{u}_i}{\partial x_j} + \frac{\partial \overline{u}_j}{\partial x_i}\right), \tag{3.1}$$

where K is the SGS eddy coefficient. At this point the reason for carrying $\tfrac{1}{3}\delta_{ij}\overline{u'_l u'_l}$ along in (2.6) and (3.1) becomes clear: to permit the left-hand side of (3.1) to become zero at each point, as does the right-hand side, when the indices are contracted (see Hinze 1959, p. 21).

Next, we shall use Smagorinsky's *et al.* (1965) assumption for K:

$$K(x, y, z, t) = (c\Delta)^2\left[\frac{\partial \overline{u}_i}{\partial x_j}\left(\frac{\partial \overline{u}_i}{\partial x_j} + \frac{\partial \overline{u}_j}{\partial x_i}\right)\right]^{\frac{1}{2}}, \tag{3.2}$$

where c is a dimensionless constant and Δ is a dimensionless, representative grid interval, here taken to be
$$\Delta = (\Delta x . \Delta y . \Delta z)^{\frac{1}{3}}. \tag{3.3}$$

The quantity in brackets in (3.2) is one-half the squared velocity deformation, and is therefore always positive.

The relationship between (3.1) and (3.3) and an inertial subrange has been neatly summarized by Leith (1968) as follows. If an inertial subrange exists on scales which encompass the grid interval, then the usual dimensional arguments demand that
$$K = c^{\frac{4}{3}}\overline{\epsilon}^{\frac{1}{3}}\Delta^{\frac{4}{3}}, \tag{3.4}$$

where $\overline{\epsilon}$ is the rate of dissipation of turbulence kinetic energy within a local grid volume. But in a numerical calculation for homogeneous turbulence, it may be shown that $\overline{\epsilon}$ is given, approximately, by

$$\overline{\epsilon} = K\frac{\partial \overline{u}_i}{\partial x_j}\left(\frac{\partial \overline{u}_i}{\partial x_j} + \frac{\partial \overline{u}_j}{\partial x_i}\right). \tag{3.5}$$

Elimination of $\bar{\varepsilon}$ between (3.4) and (3.5) then gives (3.2). An additional term should be added to the right-hand side of (3.5) for this non-homogeneous turbulence to represent an SGS triple-correlation term (see (9.2)). However, this term has been estimated to be small and has been omitted here.

It has been deduced by Lilly (1967) that, if

$$c \cong 0 \cdot 17,$$

then (2.1), (3.2)–(3.5) are compatible with the known value of Kolmogoroff's universal constant for the inertial subrange. It is understood that the finite difference form of (3.2) uses velocity differences taken over single grid intervals and that the finite-difference equations incorporate no significant internal damping or numerical instabilities. Various values of c were tested here in preliminary integrations. The value $0 \cdot 17$ turned out to be too large, causing motions to damp until excessively large mean shear built up, and causing far too much of the total turbulence energy to reside in sub-grid scales. The value

$$c = 0 \cdot 10 \tag{3.6}$$

seemed optimum and yet did not allow turbulent motions to become excessively large. This value was used in obtaining the results to be presented in § 7–§ 9.

Now it is desirable to obtain values of $\overline{u_i' u_j'}$ when $i = j$ so that they may be added to the respective resolvable turbulence intensities, and the sums compared with measurements of total averaged intensities. The SGS turbulence intensities may be obtained by horizontally averaging (3.1), given an expression for $\frac{1}{3}\overline{u_l' u_l'}$. The first-order theory of Lilly (1967) gives for this quantity

$$\tfrac{1}{3}\overline{u_l' u_l'} = \tfrac{2}{3}K^2/(c_1\,\Delta)^2, \tag{3.7}$$

with

$$c_1 = 0 \cdot 094. \tag{3.8}$$

The above value was used in this study. It should be noted that (3.1) and (3.7) essentially partition the SGS energy equally into its three parts because K in (3.2) is generally very poorly correlated with $\partial \overline{u}_i / \partial x_j$ for $i = j$.

4. The finite-difference network

The region between boundaries to be treated has a downstream length of $3h$ and a lateral width of $0 \cdot 7h$. The reason for the distinction is that the eddies were anticipated to be stretched out in the downstream direction.

The downstream length was subdivided into 24 equal grid intervals, the lateral width into 14, and the height into 20 equal grid intervals. Therefore, the three dimensionless grid intervals are

$$\Delta x = \tfrac{3}{24} = 0 \cdot 125,$$

$$\Delta y = \tfrac{0 \cdot 7}{14} = 0 \cdot 05,$$

$$\Delta z = \tfrac{1}{20} = 0 \cdot 05.$$

The total number of grid volumes used, 6720, is thus quite modest but is the

greatest number which could be conveniently stored within the high-speed memory of NCAR's CDC 6600 computer without making much greater use of memory devices having rather large access times.

The grid meshes for the different dependent variables do not coincide but are staggered in space as in Harlow & Welch (1965). Grid points at which $\overline{w}$ is stored are equally spaced between boundaries. Grid points for $\overline{P}''$ are located vertically midway between grid points for $\overline{w}$; grid points for $\overline{u}$ are located horizontally in x midway between grid points for $\overline{P}''$; grid points for $\overline{v}$ are located laterally midway in y between grid points for $\overline{P}''$. With this arrangement, the finite-difference form of the continuity equation is expressible compactly at grid points for $\overline{P}''$, which is very convenient when it comes to solving (2.7) for $\overline{P}''$.

5. Method of solving the marching equations and Poisson's equation

The 'leapfrog' method (see Fischer 1965), which has second-order accuracy in time, was utilized for the time differencing of the marching equations (2.6*a*), with respect to the advective terms in $\overline{Q}_1$. The Reynolds-stress terms were lagged in time (treated as with forward time steps) to avoid an unconditional numerical instability of the diffusion type. These terms probably helped to tie the odd and even time-step grids together so that oscillations of period $2\Delta t$, which tend to develop with the leapfrog method, grew only very slowly. To further suppress them, a forward time step was performed once each 40 time steps.

The finite-difference form used for the advective terms in (2.6*b*) is the simplest momentum and energy conserving form of Arakawa (1966) as described by Lilly (1965) for the staggered grid system. It has second-order accuracy in space and, in all cases studied by the writer, prevents non-linear numerical instability even when velocity fields contain much energy on the smallest scales. The same spatial form has also been used by Harlow & Welch (1965) and Orzsag (1968).

The dimensionless time step was set at $\Delta t = 0.0033$, a value sufficiently small to avoid the conditional numerical instability of the advective or wave type. A smaller step would have been necessary except that the co-ordinate system was moved at a constant speed in the downstream direction equal to about 0.8 of the maximum speed which developed. Such a Galilean transformation does not alter any of the governing equations, but is taken into account in §6 in the boundary condition for the *mean* flow.

In the Poisson equation for $\overline{P}''$, (2.7), the last term on the right may be expressed in temporal finite-difference form as

$$\frac{\partial}{\partial t}\left(\frac{\partial \overline{u}_i}{\partial x_i}\right)^{(n)} \simeq \left[\frac{\partial \overline{u}_i^{(n+1)}}{\partial x_i} - \frac{\partial \overline{u}_i^{(n-1)}}{\partial x_i}\right]\bigg/ 2\Delta t,$$

where $n\Delta t = t$. Here the procedure of Harlow & Welch (1965) was used of setting $\partial \overline{u}_i^{(n+1)}/\partial x_i = 0$ as it should be with incompressibility, but retaining $\partial \overline{u}_i^{(n-1)}/\partial x_i$. The reason the latter quantity was not quite zero in actuality is that (2.7) was solved by an approximate method. This procedure minimizes values of $\partial \overline{u}_i^{(n+1)}/\partial x_i$ for a given level of accuracy in the solution of (2.7) and prevents values from

building up systematically with time. The procedure works so well that it is not even necessary to have $\partial \bar{u}_i / \partial x_i = 0$ in the initial conditions!

The finite-difference form of $\nabla^2 \bar{P}''$ employed the compact 7-point operator for ∇^2. The right-hand side of (2.7) in finite-difference form was exactly compatible with the left-hand side, both being obtained directly from (2.6) by application of the finite-difference divergence operator. The approximate method used for solving (2.7) was successive point over-relaxation, with an over-relaxation coefficient of 1·6 (where 1·0 corresponds to Richardson's method of no over-relaxation). On each time step, 40 sweeps or iterations were used after the first guess which consisted of $\bar{P}''$ from the preceding time step. After each solution the condition $\langle \bar{P}'' \rangle = 0$ was enforced exactly so that $\langle \partial \bar{w} / \partial t \rangle = 0$ would be maintained exactly.

The portion of the numerical calculations of $\bar{P}''$ consumed 4·8 sec during each time step; all the other calculations consumed another 3·8 sec, and an additional 5 sec each step were consumed by frequent access to magnetic drums where various fields were temporarily stored.

6. Boundary and initial conditions

At the limits $x = 0, 3$ and at the lateral limits $y = 0, 0·7$, cyclic or repetitive boundary conditions were employed for $\bar{u}, \bar{v}, \bar{w}$, and $\bar{P}''$. This condition corresponds to the procedure in wave-number space of assigning a particular length for wave-number one.

No-slip boundary conditions cannot be employed here at the walls, because the grid interval Δz is very much larger than the height of the viscous sublayer, considering that the Reynolds number is indefinitely large. At $z = \frac{1}{2}\Delta z$, which is the distance from the wall to the first grid points for $\bar{u}$ and $\bar{v}$, the mean flow should obey the logarithmic 'law of the wall'. However, the detailed flow obeys such a law only on the average. In the absence of any known, rigorous formulation which would hold on each time step and at each grid point, the following boundary conditions have been found to work satisfactorily:

$$\frac{\partial^2 \bar{u}}{\partial z^2} = \frac{\partial^2 \langle \bar{u} \rangle}{\partial z^2} + \frac{\partial^2 \bar{u}}{\partial y^2} = -k^{-1}(\tfrac{1}{2}\Delta z)^{-2} + \frac{\partial^2 \bar{u}}{\partial y^2}, \tag{6.1a}$$

$$\frac{\partial^2 \bar{v}}{\partial z^2} = \frac{\partial^2 \bar{v}}{\partial x^2}, \tag{6.1b}$$

at $z = \frac{1}{2}\Delta z$ and $1 - \frac{1}{2}\Delta z$; and

$$\bar{w} = 0 \quad \text{at} \quad z = 0, 1, \tag{6.1c}$$

where k is von Kármán's constant of 0·4.

The horizontal average of (6.1 a) agrees with the law of the wall because the last term has zero horizontal average. Also, the second derivatives in z of $\bar{u}''$ and $\bar{v}$, where $\bar{u}'' = \bar{u} - \langle \bar{u} \rangle$, are prescribed to be locally isotropic with respect to second derivatives in y or x, respectively. It may also be seen that the boundary conditions for $\bar{u}'', \bar{v}$ and $\bar{w}$ do not involve the roughness length or the mean flow speed. This means that the dimensionless flow structure is not affected by either

a horizontal Galilean transformation or a change in roughness length, z_0, of the wall. It can be shown that the use of boundary conditions with this property, along with the non-dimensionalization by u^* and h, allows a single numerical integration to apply generally to any value of h/z_0, the only similarity parameter which is then relevant at large Reynolds number.

In (6.1 *a, b*) central differencing was used, with appropriate values of $\overline{u}$ and assigned to exterior grid points located at $z = -\frac{1}{2}\Delta z$, $1 + \frac{1}{2}\Delta z$.

Near the walls, at $z = \frac{1}{2}\Delta z$ and $1 - \frac{1}{2}\Delta z$, it is not too unreasonable to require the law of the wall,

$$\langle \overline{u} \rangle = k^{-1}\ln\left(\tfrac{1}{2}\Delta z . \frac{h}{z_0}\right), \tag{6.2}$$

to hold for the mean flow at each time step. This condition will occur only if (6.2) is prescribed initially and if $\partial\langle\overline{u}\rangle/\partial t = 0$ at these two levels subsequently. The latter condition requires known values for $(\partial/\partial z)\langle\overline{u'w'}\rangle$ in (2.6*b*) for $i = 1$ at these two levels. The latter quantity in turn requires a boundary condition on $\partial K/\partial z$ which is not available from (3.2). Also, the presence of the term

$$(\partial^2/\partial z^2)\,(\overline{w'^2} - \tfrac{1}{3}\overline{u_i'u_i'})$$

in an expansion of (2.7) requires that $\partial^2 K/\partial z^2$ be known at these two levels. These requirements were met by assuming

$$K(x,y,-\tfrac{1}{2}\Delta z,t) = bK(x,y,\tfrac{1}{2}\Delta z,t) \tag{6.3}$$

at exterior grid points, where b is a constant chosen such that

$$\partial\langle\overline{u}\rangle/\partial t = 0 \quad \text{at} \quad z = \tfrac{1}{2}\Delta z. \tag{6.4}$$

Relationships analogous to (6.3, 6.4) also apply at $z = 1 - \frac{1}{2}\Delta z$. Typical values of b which resulted, -0.3, imply that $\partial K/\partial z > 0$ at $z = \frac{1}{2}\Delta z$.

The term $(\partial^2/\partial z^2)\,(\overline{w'^2} - \tfrac{1}{3}\overline{u_i'u_i'})$ occurring in an expansion of (2.7) also requires that $\partial^3\overline{w}/\partial z^3$ be known at $z = \frac{1}{2}\Delta z$ and $1 - \frac{1}{2}\Delta z$. Since the $\overline{w}$ grid points are located at $z = 0, \Delta z, 2\Delta z, \ldots$, this requirement necessitates the specification of $\overline{w}$ values at exterior $\overline{w}$ grid points located at $z = -\Delta z$ and $1 + \Delta z$. These were assigned so that the equation of continuity would be compactly satisfied at the exterior grid points of $\overline{P}''$ located at $z = -\frac{1}{2}\Delta z$ and $1 + \frac{1}{2}\Delta z$. Values of pressure at the latter points were assigned to satisfy the horizontal boundary conditions on $\partial\overline{P}''/\partial z$ which stem directly from (2.6) for $i = 3$.

After completion of this study, it was realized that the correct expression for $\partial^3\overline{w}/\partial z^3$ centred at $z = \frac{1}{2}\Delta z$ and $1 - \frac{1}{2}\Delta z$ should be obtained from differentiation of (2.3):

$$\frac{\partial^3\overline{w}}{\partial z^3} = -\frac{\partial}{\partial x}\left(\frac{\partial^2\overline{u}}{\partial z^2}\right) - \frac{\partial}{\partial y}\left(\frac{\partial^2\overline{v}}{\partial z^2}\right).$$

The initial conditions for $\overline{u}''$ were random except that the finite-difference continuity equation was obeyed. This requirement, which turned out to be unnecessary, was accomplished by use of a three-dimensional vector potential (Aziz & Hellums 1967) having random components. The initial magnitudes of the velocity components were about twice as large in magnitude as those observed experimentally by Laufer (1950).

About 1000 time steps were required before the $\bar{u}$ eddies reached typical equilibrium patterns of great elongation in the x direction. Subsequently, some experimenting was done with the horizontal boundary conditions, with the value of c in (3.2), the value of Δy, and the initial mean wind profile. Usually the initial condition was taken as the velocity structure which emerged from the preceding trial integration. Therefore, for the cases to be presented in the next sections for which $c = 0\cdot10$ and $\Delta y = 0\cdot05$, the initial conditions were almost as representative of typical velocity structures as subsequent results. The random 'starting' initial conditions previously mentioned are thus scarcely relevant to this particular study.

7. Calculated mean flow profiles

Dimensionless mean flow profiles which evolved under the influence of the Reynolds stress $\langle \overline{uw} + \overline{u'w'} \rangle$ are shown in figure 1(a) at four widely different times. The end-points at $z = \frac{1}{2}\Delta z$ and $1 - \frac{1}{2}\Delta z$ agree with the measured profile of Laufer (1950) (for which $\frac{1}{2}hu^*u_{\max}/\nu = 61{,}600$) because of assumptions (6.2, 6.3) for $(\partial/\partial z)\langle \overline{u'w'} \rangle$ at these levels, and because h/z_0 was prescribed the same as in Laufer's experiment, about $8\cdot8 \times 10^4$.

In figure 1(b), the average of 10 profiles of $\langle \bar{u} \rangle$ at widely spaced times of integration is shown along with Laufer's profile. The dimensionless time interval between individual profiles before averaging is $0\cdot70$ (208 time steps), so that the result is essentially an ensemble average. In addition, profiles for the lower and upper channels have been averaged together.

Aside from the general shape of the mean profile, the agreement with the measured profile is not very good. The excessive calculated flow speeds imply that a smaller K should be used so that a smaller mean shear would support the proper value of resolvable stress. Yet, if K is decreased by decreasing c in (3.2) below a value of about $0\cdot08$, excessively large turbulence intensities $\langle \bar{u}''^2 \rangle$ and $\langle \bar{v}^2 \rangle$ are the result. The answer to this dilemma may require the abandonment of the use of the eddy coefficient and the employment of transport equations for the SGS Reynolds stresses (Lilly 1967).

One may question the comparison here of the calculated profiles for very large Reynolds numbers with that measured at a modest Reynolds number. Only at very large Reynolds number is the shape of the interior 95% of the flow truly independent of Reynolds number. However, the actual profile shape at Reynolds numbers much larger than those employed by Laufer is unlikely to be *less* flat in the central region than his measured profile. The discrepancy between calculated and measured mean profiles thus appears to be real.

Since nothing but the mean flow profile is affected by a change in h/z_0 (see (2.6) and (6.1, 6.2), and that in a known way (see (6.2)), this model gives for a drag coefficient C_D the following functional relationship:

$$C_D^{-\frac{1}{2}} = \langle \bar{u} \rangle_{\max} = k^{-1}\left[\ln\left(\frac{h}{z_0}\right) - A' \right], \tag{7.1a}$$

where
$$A' = -0\cdot7 \tag{7.1b}$$

from the numerical results presented and for $k = 0.4$. Because of the discrepancy just mentioned, the value of $C_D^{\frac{1}{2}}$ obtained here, 0.033, is 10% smaller than that obtained by Laufer of 0.037. (In rendering Laufer's mean wind profile dimensionless at his largest Reynolds number, his value of u^* measured from the pressure drop and from the wall shear was used in preference to a smaller value measured by X-wire anemometry.)
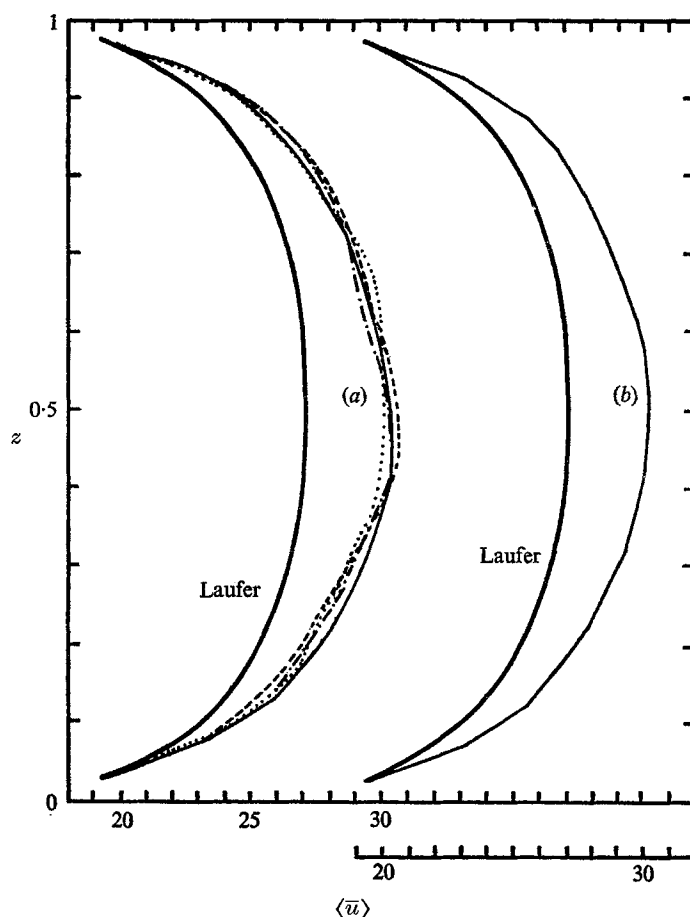

FIGURE 1. Calculated and measured mean wind profiles (made dimensionless by u^*). Thin curves in (a) were calculated at four widely separated times between $t = 0$ and $t = 7.41$. Thin curve in (b) is the average of 10 such profiles. Heavy curve is from Laufer (1950).

8. Detailed flow patterns

(i) *Examination of an x–z plane*

The x–z plane at $y = 4\Delta y$, as well as two other planes of the motion, was examined periodically for its flow structure. Figure 2 shows typical patterns of $\bar{u}''$, $\bar{w}$, $\bar{v}$ and $\bar{P}''$ on the ninth of the 10 consecutive periods ($t = 6.71$).

A generally positive correlation between $\bar{u}$ and $\bar{w}$ is barely discernible in the upper half channel, and a negative correlation in the lower half. These enable

the transfer of resolvable momentum outward towards the walls. Near the walls, much of the momentum is carried by the SGS motions whose magnitudes will be examined in the next section.
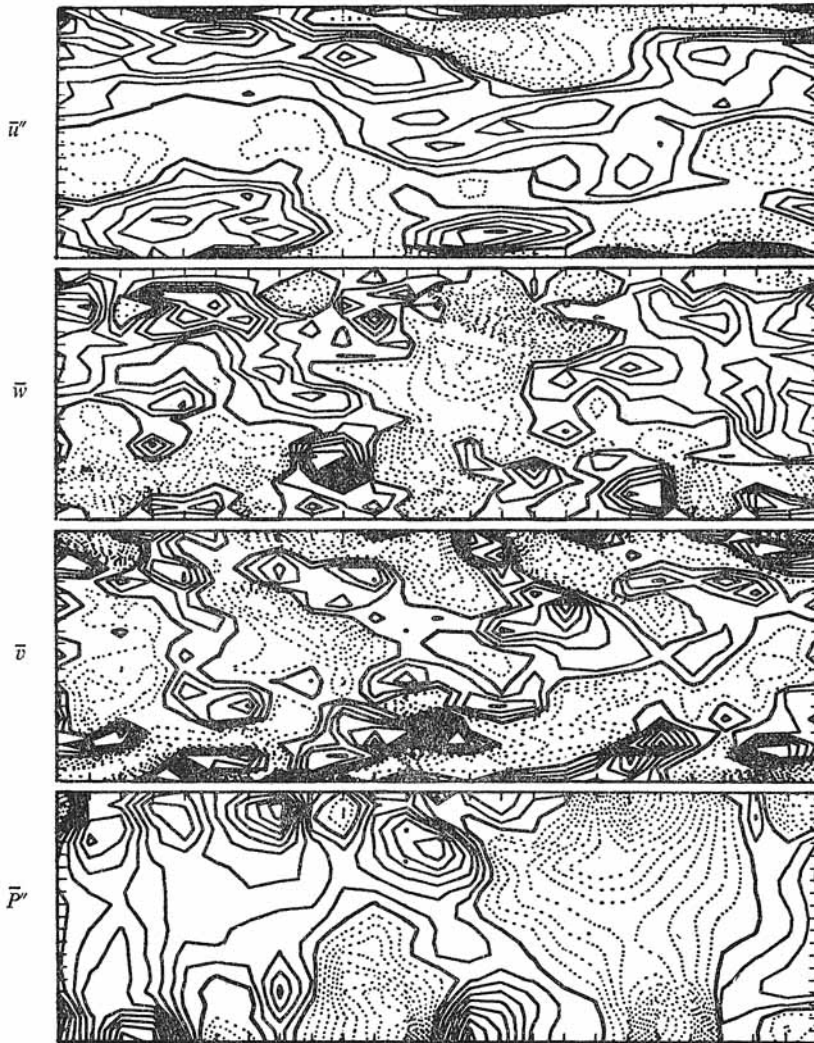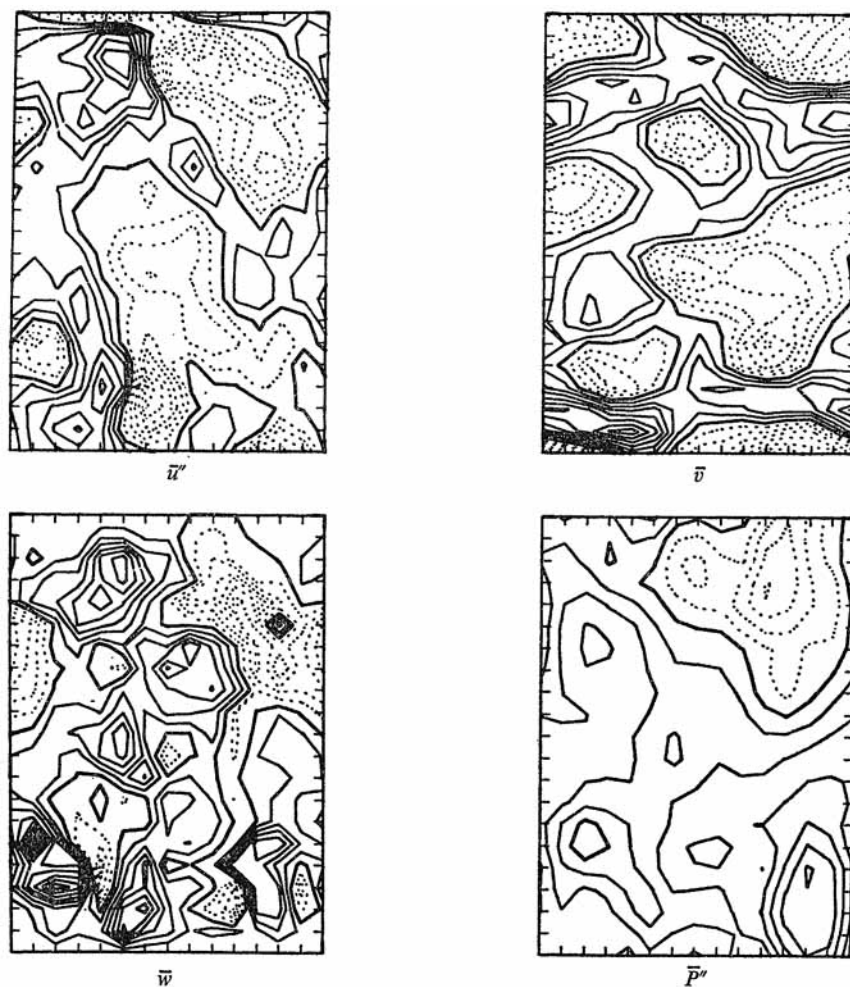

Isopleths in x–z plane at time $= 6.71$

FIGURE 2. Contours of velocity components $\bar{u}''$, $\bar{w}$, $\bar{v}$ and of pressure $\bar{P}''$ in an x–z plane. Positive values are contoured by thin solid isopleths, zero values by a heavier contour, and negative values by dotted contours. The dimensionless contour interval is 0.5 for $\bar{u}''$ and $\bar{P}''$, and 0.25 for $\bar{w}$ and $\bar{v}$. Tick marks along edges indicate the grid intervals. Values of $\bar{u}''$, $\bar{v}$ and $\bar{P}''$ have been centred to coincide with grid-point locations of $\bar{w}$.

The greater elongation of the $\bar{u}$ eddies in the downstream direction than of $\bar{v}$ or $\bar{w}$ is perhaps the most distinguishing result of the calculations. It is interesting that the $\bar{w}$ eddies are not notably elongated even though the correlation between $\bar{w}$ and $\bar{u}$ has a magnitude near 0.3 or 0.4.

The $\bar{u}$ and $\bar{v}$ eddies have pronounced downstream tilts toward the walls. The angle of the tilt away from the vertical is typically in the neighbourhood of $80°$ for $\bar{u}''$ and $60°$ for $\bar{v}$. Downstream tilts are scarcely evident in the $\bar{w}$ eddies. Since the tilting of an eddy structure is probably caused by mean shear, these results imply that the typical lifetime of a $\bar{u}''$ eddy is larger than that of a $\bar{v}$ eddy while that of a $\bar{w}$ eddy is smaller.

Isopleths in *y–z* plane at time $= 6\cdot71$

FIGURE 3. Contours of $\bar{u}''$, $\bar{w}$, $\bar{v}$ and $\bar{P}''$ in a *y–z* plane. See caption of figure 2 for other details.

Pressure fluctuations can be seen to have maxima centred close to the boundaries. These can often be traced to the term $2(\partial \bar{w}/\partial x)(\partial \bar{u}/\partial z)$ in an expansion of (2.7), since $|\partial \langle \bar{u} \rangle / \partial z|$ is much larger near the boundaries than any of the other filtered velocity gradients. In particular, very near the lower boundary the pressure centres in figure 2 tend to have the sign of $\partial \bar{w}/\partial x$. The pressure eddies show no indication of downstream elongation or tilt.

(ii) *Examination of a y–z plane*

The same four variables at the same time are shown for the y–z plane, $x = 4\Delta x$, in figure 3. The correlations between $\overline{u}$ and $\overline{w}$ show up more clearly in this plane, and the circulations which transport the resolvable momentum vertically are frequently contained mainly in y–z planes. A good example occurs in the upper right portion where the reversal of the $\overline{v}$ flow centred at $(12\Delta y, 17\Delta z)$ completes the circulation shown at this location of the $\overline{w}$ flow. Examination of $\overline{u}'' = \overline{u} - \langle \overline{u} \rangle$ in this region shows that this counter-clockwise rotating vortex (facing upstream) is transporting momentum towards the upper wall. It is evident that a particle within this vortex would transcribe a helical path while travelling downstream. Such helical vortices have been observed in the atmospheric boundary layer by Angell, Pack & Dickson (1968).

It is not surprising that in figure 3 there is a pressure minimum existing near the centre of this vortex. The minimum is associated with the term $2(\partial \overline{v}/\partial z)(\partial \overline{w}/\partial y)$ in an expansion of (2.7). When this term tends to be strongly negative because of the circulation, $\nabla^2 \overline{P}''$ tends to be positive and $\overline{P}''$ negative.

(iii) *Examination of an x–y plane*

Motions in the horizontal plane located at $z = \frac{7}{2}\Delta z = 0\cdot 175$ are shown in figure 4. The elongation of the $\overline{u}$ eddies is seen to be very pronounced at this level. The shape is of a very irregular river of higher speed fluid (lower portion of upper picture) embedded in slower moving fluid. The fact that only one such high speed river usually existed within the limits of y, and that its sign generally did not change in x, represents serious restrictions imposed by the limited physical extent of the region treated.

Close inspection of figure 4 also shows that maxima in $\overline{u}''$ (gusts) tend to have sharper leading edges (downstream edges) than trailing edges. Thus the skewness $\langle (\partial \overline{u}/\partial x)^3 \rangle / \langle (\partial \overline{u}/\partial x)^2 \rangle^{\frac{3}{2}}$ is negative. The average value at this level from the ensemble of 10 cases is $-0\cdot 37$, increasing to $-0\cdot 52$ at $z = \frac{3}{2}\Delta z$. It is interesting that the same quantity without overbars is also negative, having a value of about $-0\cdot 5$ in grid-produced turbulence (see e.g. Uberoi 1963). The skewness of $\partial \overline{v}/\partial y$ turned out to have an average value of $-0\cdot 17$ at $z = \frac{7}{2}\Delta z$, while that of $\partial \overline{w}/\partial z$ at this level was $+0\cdot 17$.

The irregularity of these computer drawn figures is somewhat misleading on small scales because the contour plotting program was linear. Examination of longitudinal velocity spectra showed that there was no excess of energy on scales of $2\Delta x$.

9. Turbulence statistics

(i) *Turbulence intensities and Reynolds stress*

Vertical profiles of the three resolvable turbulence intensities $\langle (\overline{u}'')^2 \rangle$, $\langle \overline{v}^2 \rangle$, and $\langle \overline{w^2} \rangle$, and the resolvable mean Reynolds stress $\langle \overline{uw} \rangle$ are shown in the upper half of figure 5 at time $6\cdot 71$ by the thin curves. The heavy curves are the measurements of Laufer (1950) made dimensionless by u^{*2} at his largest Reynolds number.

30   FLM 41

Near the walls the curves turn back towards zero because there much of the turbulence intensity is associated with the SGS motions. The average SGS kinetic energy obtained from (3.7) was partitioned (nearly equally) by (3.1) and added to the resolvable turbulence intensities to obtain the three lower-left-hand portions of figure 5. The addition of the SGS contributions improves the shapes somewhat near the boundaries, and adds little energy elsewhere.
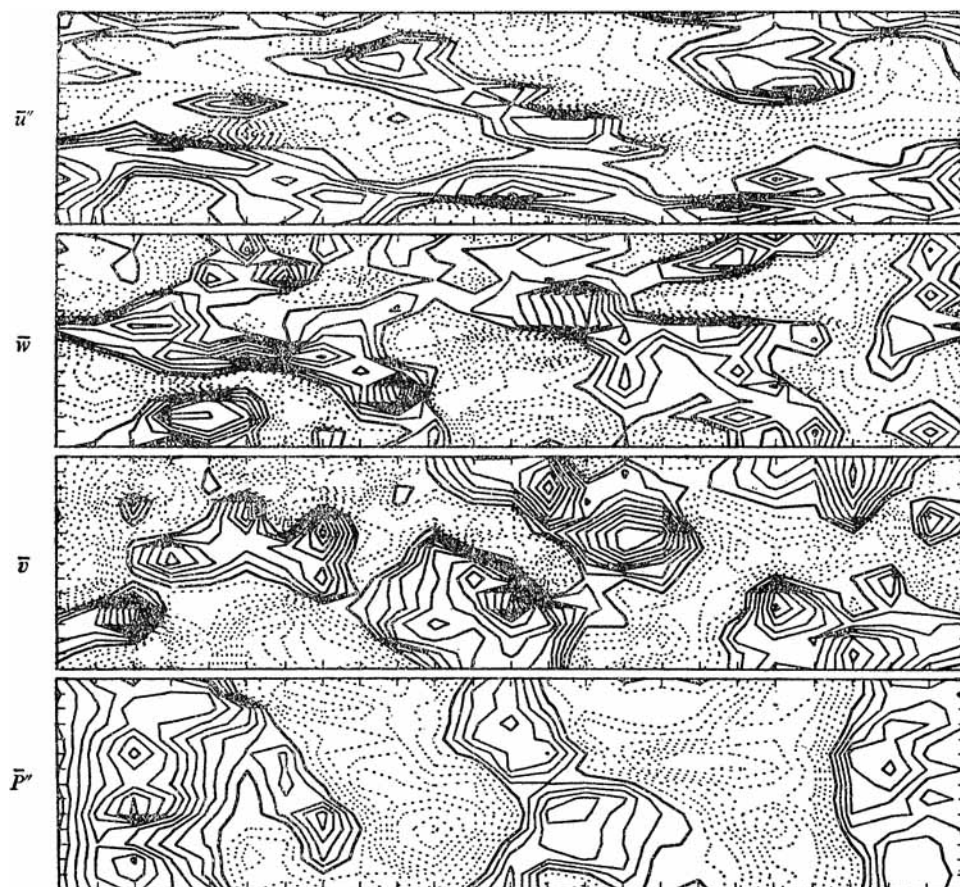
Isopleths in x–y plane ($z = 0.18$) at time $= 6.71$

FIGURE 4. Contours of $\bar{u}''$, $\bar{w}$, $\bar{v}$ and $\bar{P}''$ in the x–y plane at $z = 0.175$. See caption of figure 2 for other details.

The total Reynolds stress, lower right, was formed by adding

$$\left\langle -K\left(\frac{\partial \bar{u}}{\partial z} + \frac{\partial \bar{w}}{\partial x}\right)\right\rangle \quad \text{to} \quad \langle \overline{uw}\rangle.$$

Of necessity it fluctuates about the correct equilibrium value, $-1 + 2z$ (heavy line) because of the interaction between the mean wind and the mean Reynolds stress. That is, an approximately steady mean wind is only obtained after the total Reynolds stress has approximately reached the equilibrium shape which balances

the gross downstream pressure gradient. Therefore the calculated distribution of dimensionless mean Reynolds stress can in no way be used to verify the numerical results.
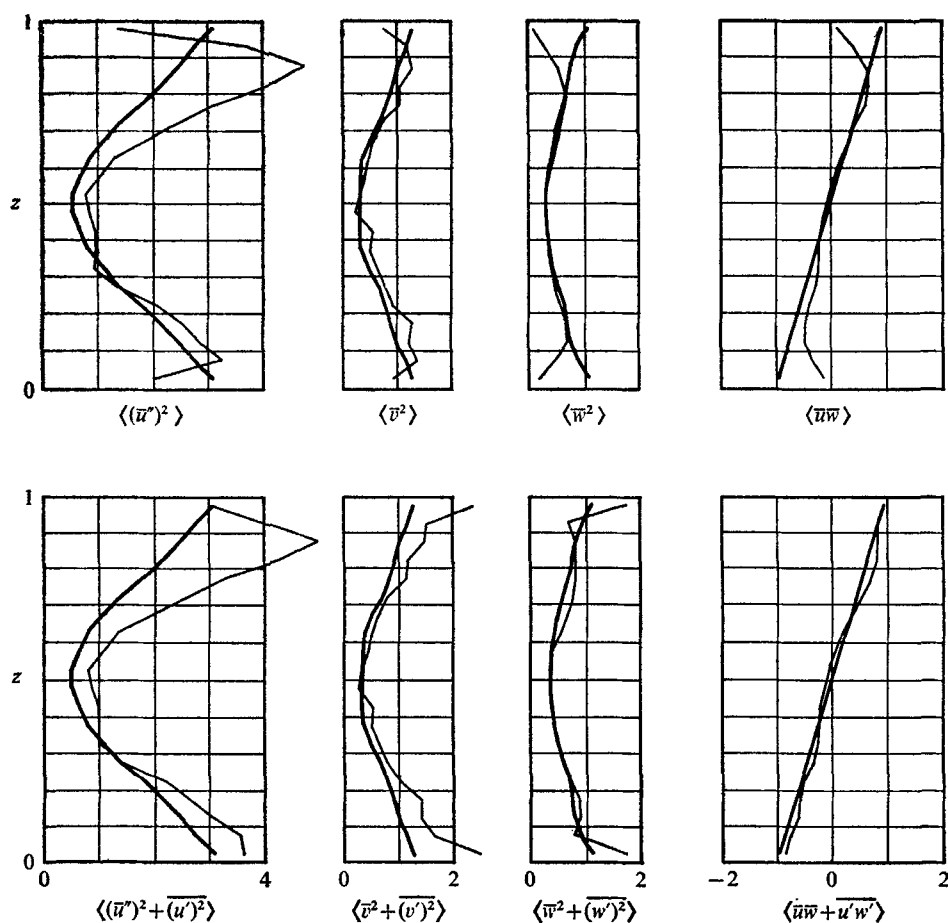

FIGURE 5. Vertical profiles of dimensionless, horizontally averaged turbulence intensities and Reynolds stress (thin curves). Upper portion shows the resolvable turbulence intensities and $\langle \overline{uw} \rangle$; lower portion the total intensities after adding in the subgrid scale estimates. Heavy curves are from the measurement of Laufer (1950).

Profiles of total dimensionless turbulence intensities averaged from the 10 sets of data and over both halves of the channel are presented in figure 6. It appears from the deficiency in longitudinal turbulence intensity very near the boundaries that a larger portion of the SGS kinetic energy should have been allotted to the longitudinal component and correspondingly less to the lateral and vertical components. That is, a modification to (3.1) which would allow anisotropy of the SGS intensities is desirable. The profiles of $\langle \overline{v^2} + \overline{v'^2} \rangle$ and $\langle \overline{w^2} + \overline{w'^2} \rangle$ are not similar enough to each other, but generally differ from the measurements by only $\pm 30\%$ or less except at the first interior grid points. However, the profile of total longitudinal intensity is systematically larger than Laufer's by about 50%. The

30-2

overestimate may not be real if his measurements of $(u - \overline{u})^2$ averaged in time had suffered from lack of low frequency response to the elongated u eddies. Later measurements of this quantity which have been reported for atmospheric boundary turbulence and wall turbulence of pipe flow by Lumley & Panofsky (1964) are larger and range from 4·4 to 8·4.
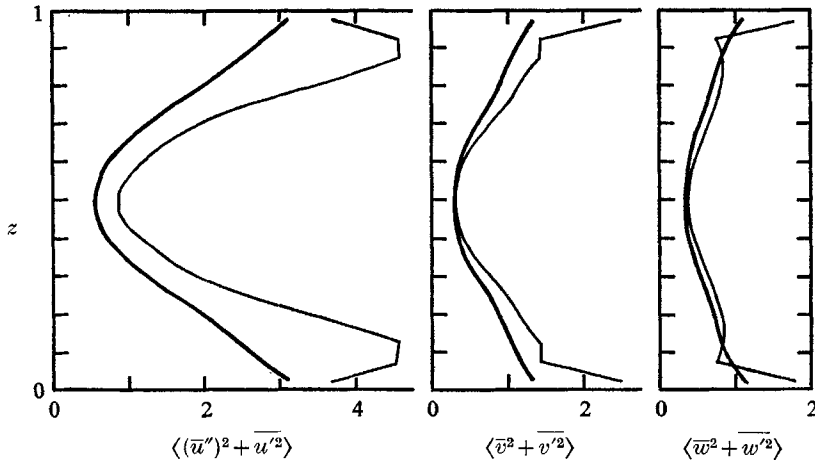

FIGURE 6. Averaged vertical profiles of the total turbulence intensities from the ensemble of results, thin curves, and from Laufer's measurements, heavy curves.

The total correlation coefficient, C_{uw}, defined by

$$C_{uw} = \langle \overline{uw} + \overline{u'w'} \rangle / [\langle (\overline{u}'')^2 + \overline{u'^2} \rangle \langle \overline{w^2} + \overline{w'^2} \rangle]^{\frac{1}{2}}$$

is shown in figure 7 for the numerical calculations by the solid line. It agrees well with that presented by Laufer (dashed line) at his largest Reynolds number. However, it appears that Laufer utilized his X-wire measurements of Reynolds stress, rather than the somewhat different distribution compatible with the measured downstream pressure gradient and measured wall shear, to obtain his correlation coefficients. Using the latter distribution, which is consistent with the wall stress previously employed for non-dimensionalization, the dash-dot profile in figure 7 is obtained. In comparison with this profile, the numerically calculated values of $-C_{uw}$ are too small because $\langle (\overline{u}'')^2 + \overline{u'^2} \rangle$ of figure 6 is too large.

(ii) *The tubulence kinetic-energy balance*

The energy balance for the statistically steady state may be expressed as

$$\langle \bar{\epsilon} \rangle = -\langle \overline{uw} + \overline{u'w'} \rangle \frac{\partial \langle \overline{u} \rangle}{\partial z} - \frac{\partial}{\partial z} \left\langle \overline{w} \frac{\overline{u_l'' u_l''}}{2} \right\rangle - \frac{\partial}{\partial z} \langle \overline{w} \overline{P''} \rangle - \frac{\partial}{\partial z} \left\langle \overline{w' \left(\frac{u_l' u_l'}{2} + \frac{p'}{\rho_0 u^{*2}} \right)} \right\rangle. \quad (9.1)$$

This expression for the rate of dissipation is different from the horizontal average of (3.5) because the latter represents the explicit rate of cascade of energy from resolvable scales to subgrid scales. The two must be equivalent, however. The

last term in (9.1) is an SGS effect which, following Lilly (1967), may be related to an eddy diffusion of SGS energy

$$-\frac{\partial}{\partial z}\left\langle \overline{w'\left(\frac{\overline{u_l' u_l'}}{2}+\frac{p'}{\rho_0 u^{*2}}\right)}\right\rangle = \frac{\partial}{\partial z}\left\langle K\frac{\partial}{\partial z}\left(\frac{\overline{u_l' u_l'}}{2}\right)\right\rangle, \qquad (9.2)$$

where $\overline{u_l' u_l'}$ is given by (3.7). It is assumed that K in (9.2) is the same as K in (3.2).
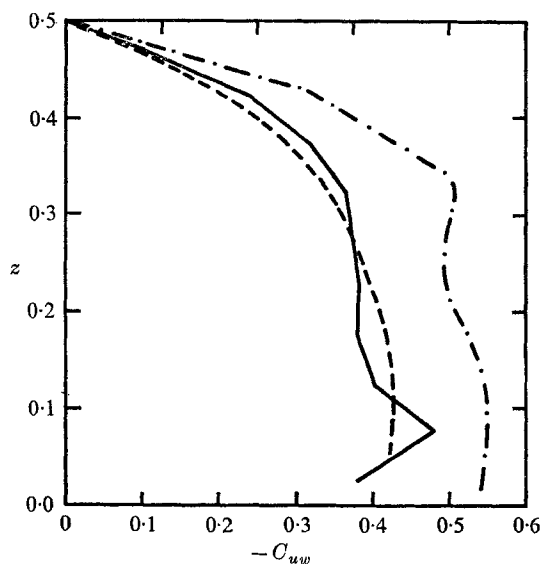
FIGURE 7. Vertical profiles of the correlation coefficient between w and u. Thin solid curve is the average calculated profile from the model; dashed line is the profile presented by Laufer; dash-dot line is Laufer's profile derived from stress measurements not involving X-wire anemometry.

The terms in (9.1) averaged from the 10 cases, and averaged over both halves of the channel, are shown in figure 8. The rate of dissipation nearly balances the rate of production, $-\langle \overline{uw}+\overline{u'w'}\rangle(\partial\langle\overline{u}\rangle/\partial z)$, except in the region $0\cdot4 < z < 0\cdot6$. (This result differs from Laufer's rather qualitative estimate that ϵ is about $\frac{1}{2}$ the rate of production between $0\cdot1 < z < 0\cdot3$. In a later study of turbulent pipe flow, however, Laufer (1954) found a much closer balance between the two.) It is disappointing that the eddy transfer terms

$$-\frac{\partial}{\partial z}\left\langle \overline{w}\,\frac{\overline{u_l'' u_l''}}{2}\right\rangle \quad \text{and} \quad -\frac{\partial}{\partial z}\langle \overline{w}\overline{P}''\rangle$$

do not have greater statistical reliability. However, it appears that in the region $0\cdot025 < z < 0\cdot4$ the kinetic energy diffusion rate,

$$\left|-\frac{\partial}{\partial z}\left\langle \overline{w}\,\frac{\overline{u_l'' u_l''}}{2}\right\rangle\right|,$$

is generally less than $0\cdot1\langle\overline{\epsilon}\rangle$, with the 'pressure-energy' diffusion rate,

$$\left|-(\partial/\partial z)\langle \overline{w}\overline{P}''\rangle\right|,$$
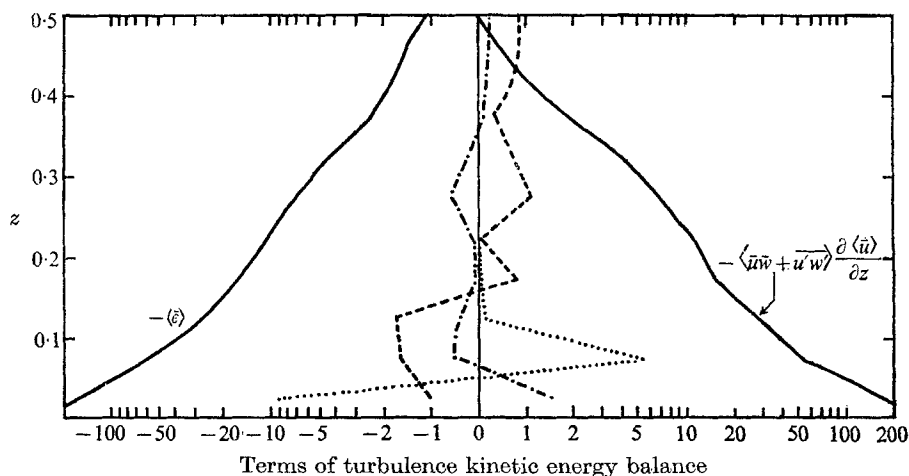
being smaller yet.

FIGURE 8. Average vertical profiles of numerically calculated terms of the turbulence kinetic-energy balance equation. Note change in scale in abscissa from linear to logarithmic at ± 1. ----, $(\partial/\partial z)\langle -\tfrac{1}{2}\overline{w u_i'' u_i''}\rangle$; $\cdots\cdots$, $(\partial/\partial z)\langle -\overline{w'\{\tfrac{1}{2}u_i'u_i'+(p'/\rho_0 u_*^2)\}}\rangle$; —·—·—, $(\partial/\partial z)\langle -\overline{wP}\rangle$.
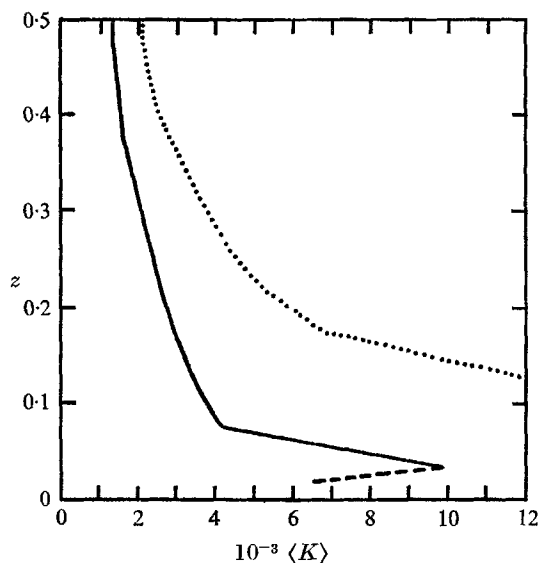

FIGURE 9. Averaged vertical profile of K, solid line. Dotted line is the profile that results if the grid volume is increased eightfold (see §10(ii)).

The SGS energy diffusion rate, (9.2), which may be seen to be nearly proportional to $(\partial^2/\partial z^2)\langle K\rangle^3$, is significant only for $z < 0\cdot 1$. Since $\langle K\rangle$ had the average profile given in figure 9, the large negative values come from the negative curvature of $\langle K\rangle^3$ at its peak at $z = 0\cdot 025$, with the large positive values centred at $z = 0\cdot 075$ being associated with reversed curvature there. Except for this large positive value, which probably cannot be trusted because of uncertainty of assumptions (9.2) and (3.2), the production rate of turbulence kinetic energy exceeds $\langle\bar\epsilon\rangle$ below $z = 0\cdot 15$ with the opposite occurring above.

(iii) *Pressure fluctuations and transfers towards isotropy*

The average vertical profile of the resolvable root-mean-square pressure fluctuation, $\langle(\overline{P}'')^2\rangle^{\frac{1}{2}}$, is shown in figure 10. For comparison, the total turbulence kinetic energy obtained from figure 6 is included. The pressure fluctuation is more uniform with height than the energy, and averages $0\cdot85$ of it. For isotropic turbulence, this fraction would correspond to $\frac{3}{2}$ $(0\cdot85) = 1\cdot28$ of $\langle u^2\rangle$ or slightly larger if an estimate of the SGS contribution $\langle(p'/\rho_0 u^{*2})^2\rangle^{\frac{1}{2}}$ were included. The ratio measured by Uberoi (1954) for isotropic turbulence is $0\cdot7$. There is no reason to believe, however, that the two should be the same.
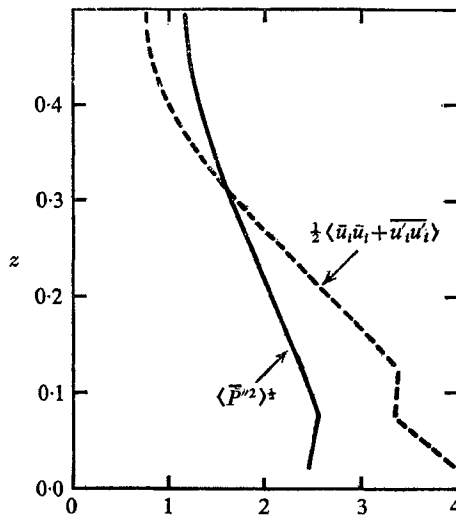

FIGURE 10. Averaged vertical profile of resolvable root-mean-square pressure fluctuation, solid curve, and total calculated turbulence kinetic energy, dashed curve.

It is interesting to examine the terms $\langle\overline{u}\,\partial\overline{P}''/\partial x\rangle$, $\langle\overline{v}\,\partial\overline{P}''/\partial y\rangle$, and $\langle\overline{w}\,\partial\overline{P}/\partial z\rangle$, along with the pressure and velocity patterns, to see how the energy is transferred from the $\overline{u}$ component to $\overline{v}$ and $\overline{w}$. Where the former transfer term is positive and the latter two negative it indicates a transfer in this sense. Averaged vertical profiles of these terms are shown in figure 11. The transfer was in this direction at all levels, with greatest resolvable transfer away from $\overline{u}''$ occurring at $z = \frac{3}{2}\Delta z$ where $|\overline{P}''|$ and $|\overline{u}''|$ were largest. The small residual of the three terms is $(\partial/\partial z)\langle\overline{w}\overline{P}''\rangle$, the negative of which forms a small part of the energy balance in figure 8.

(iv) *One-dimensional autocorrelation coefficients*

Autocorrelation coefficients, defined by

$$R_{ij}(z,\mathbf{r}) = \langle\overline{u}_i''(\mathbf{x})\,\overline{u}_j''(\mathbf{x}+\mathbf{r})\rangle/\{\langle[\overline{u}_i''(\mathbf{x})]^2\rangle\,\langle[\overline{u}_j''(\mathbf{x}+\mathbf{r})]^2\rangle\}^{\frac{1}{2}}, \qquad (9.3)$$

where $\mathbf{x} = \mathbf{i}x+\mathbf{j}y+\mathbf{k}z$ is the position vector and $\mathbf{r} = \mathbf{i}r_x+\mathbf{j}r_y+\mathbf{k}r_z$ is the displacement vector, have been averaged over the ensemble of 10 cases and are presented in figures 12 and 13 for $j = i = 1, 2, 3$ (no summation). Note that the

correlations in (9.3) are with respect to the *horizontal* mean rather than individual *line* means. This procedure more closely simulates the experimental method of obtaining autocorrelations with respect to time means, because the horizontal mean values of this study are approximately ergodic whereas individual line means are not. The distinction is only important, however, for $R_{11}(z, r_x)$.
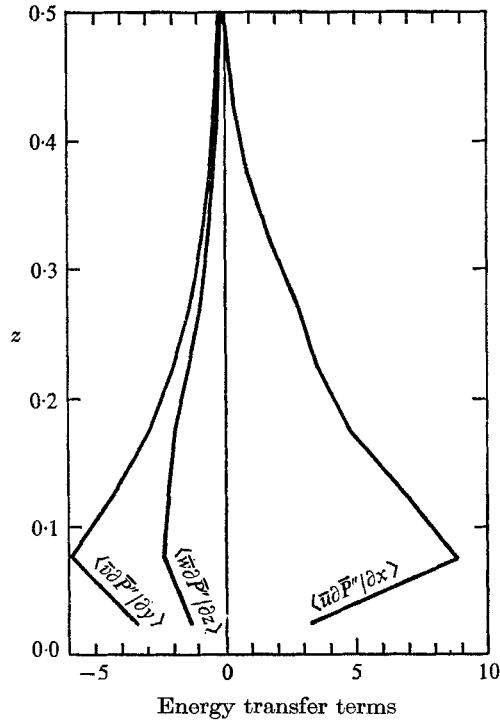

FIGURE 11. Averaged vertical profiles of the rate of transfer of resolvable energy from $\langle \overline{u}''^2 \rangle$ to $\langle \overline{v}^2 \rangle$ and $\langle \overline{w}^2 \rangle$.

Both figures show that the autocorrelation which drops off least rapidly is for the velocity component in the direction of the displacement. This is the effect of the continuity equation.

Figure 12 for $R_{ii}(z, r_x)$ clearly shows how the $\overline{u}$ eddies are elongated with respect to $\overline{v}$ and $\overline{w}$. Values of $R_{22}(z, r_x)$ and $R_{33}(z, r_x)$ cross zero at about $r_x = 2\Delta x$, which implies that the dominant wavelength in x of $\overline{v}$ and $\overline{w}$ is only about $8\Delta x = 1$. This result agrees with estimates which can be made from figure 4.

The autocorrelation does not necessarily reach zero or become negative in this study because the cyclic boundary conditions allow the zero wave-number, or non-zero constant value, to occur along a line. This effect simulates eddies of much greater length, and is seen to occur significantly for $R_{11}(0.20, r_x)$ in figure 12. If $\mathbf{r}$ in (9.3) and in figures 12, 13 were lengthened to include $r_x = 3$ and $r_y = 0.7$, these autocorrelation coefficients would climb symmetrically back up to unity.

In figure 13(a) for $R_{11}(z, r_y)$, thin solid lines, comparison may be made with Laufer's measurements, heavy curves, of this quantity. The more rapid decrease of the calculated autocorrelations from unity may reflect the restriction $0 \leqslant y \leqslant 0.7$. A greater lateral width would allow some wider eddies to exist.
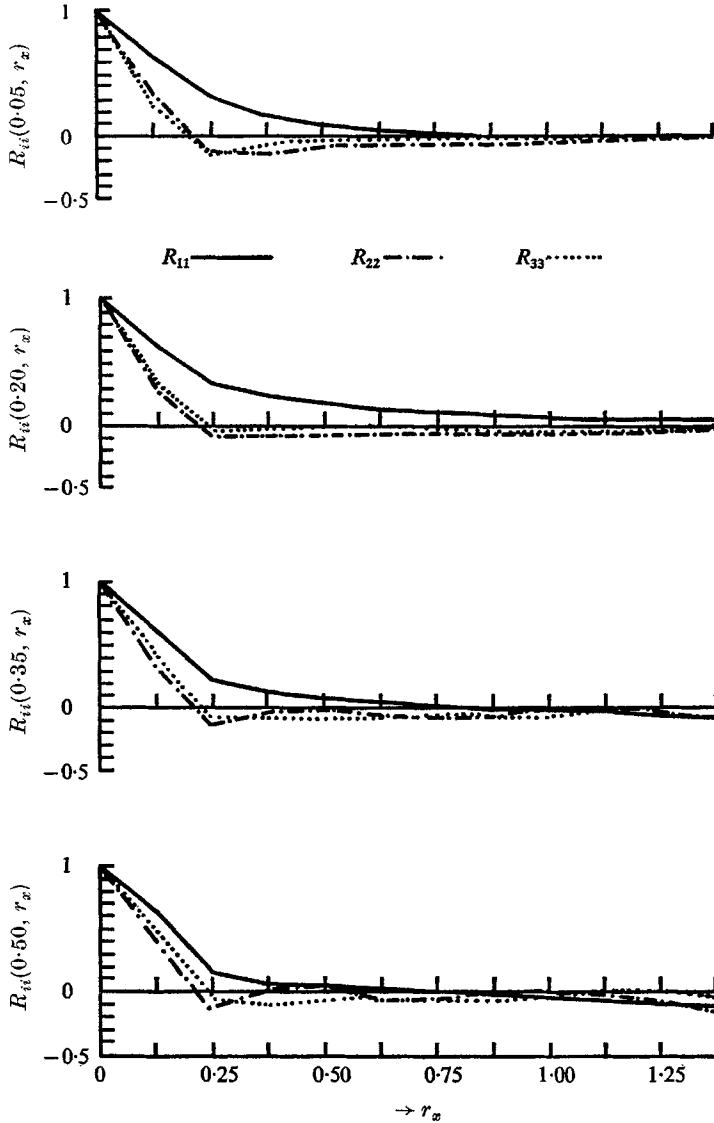

FIGURE 12. Autocorrelation coefficients in x defined by (9.3) at the levels 0·05, 0·20, 0·35, and 0·50 (from top to bottom). R_{11} (solid line) is for the $\bar{u}$ component, R_{22} (dash-dot) for $\bar{v}$, and R_{33} (dotted) for $\bar{w}$. The displacement scale is at the bottom, and the intervals between tick marks are grid intervals.

These would contribute towards increased correlations at small and moderate r_y. This interpretation is not unambiguous as the zero wave-number is permitted in y. But in figure 4 and at all other times these planes were examined, there was no tendency for the $\bar{u}$ eddies to have the same sign over all y.

In figure $13(b)$ the comparison of the calculated $R_{11}(z, r_z)$ with Laufer's measurements shows somewhat closer agreement except at the lowest level. This may be because there is no arbitrary restriction placed upon the maximum vertical scales of motion in the model.
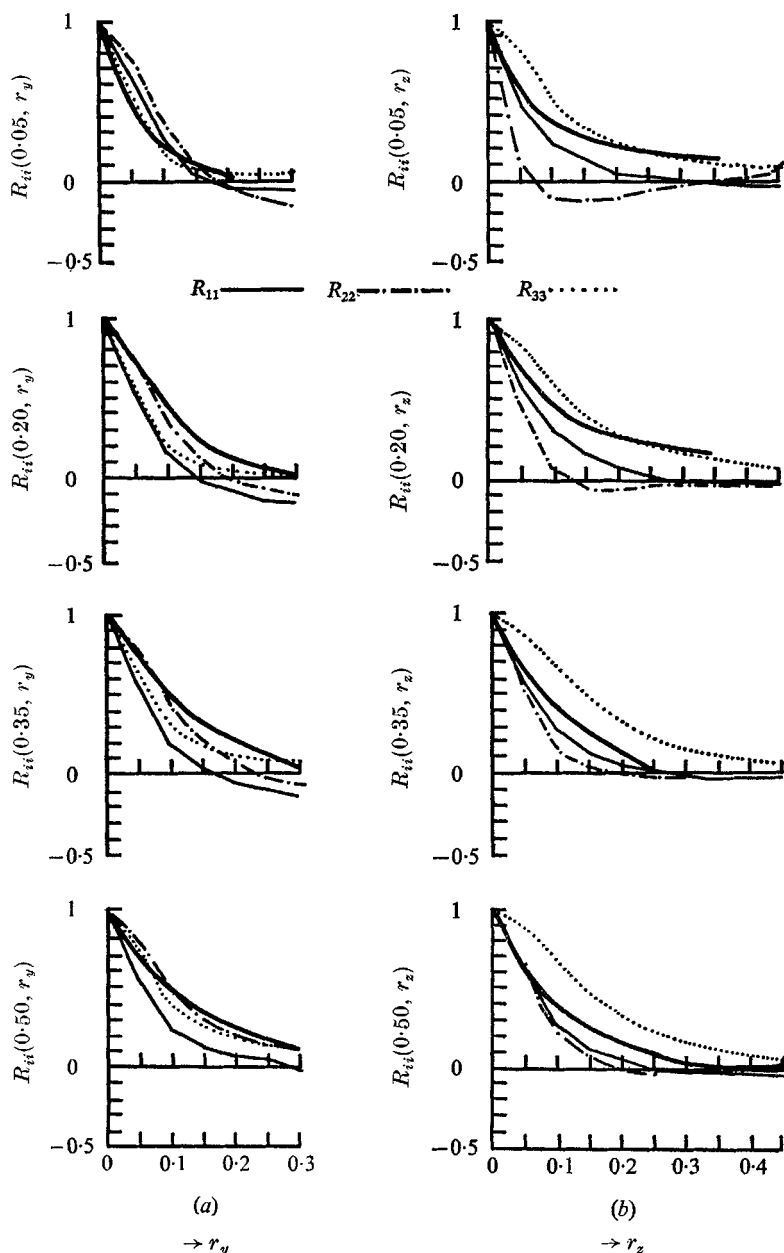

FIGURE 13. Autocorrelation coefficients in y, (a), and in z, (b). The heavy solid curves are from Laufer's measurements. See caption of figure 12 for other details.

After this study was completed, the work of Comte-Bellot (1965) on plane Poiseuille flow came to my attention. A comparison of the numerical results with those at her largest Reynolds number (either 240,000 or 460,000, based upon full channel height) gives the following changes. The discrepancy in the mean flow profile is reduced by 40 %; the overestimate in the longitudinal turbulence intensity is eliminated, although the other two turbulence intensities are then underestimated by about the same amount (30 %) as they had been overestimated using Laufer's data; the correlation coefficient C_{uw} agrees very closely with Comte-Bellot's, which essentially follows the dashed curve of figure 7; the auto-correlation coefficients in y and z (figure 13) generally agree more closely than with Laufer's; and the slow decay of R_{11} in the x direction (figure 12), especially at $z = 0.20$, is confirmed.
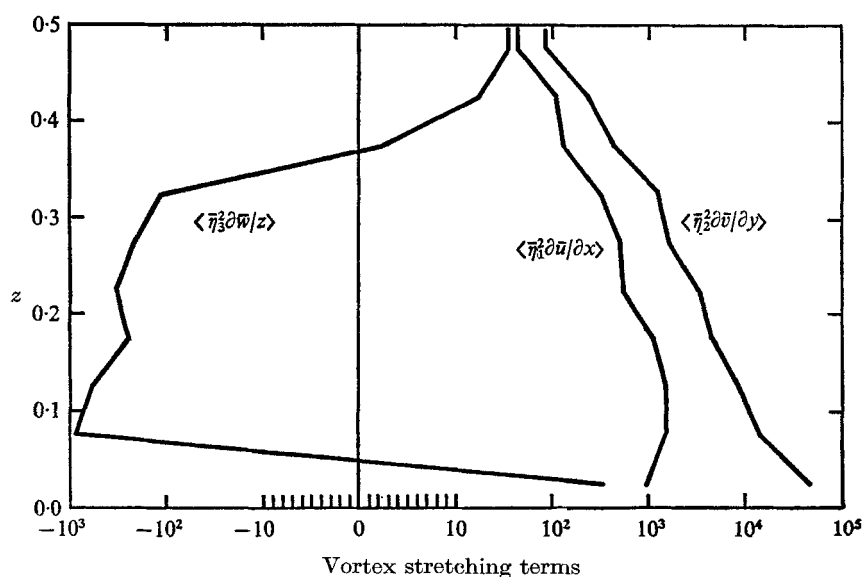

FIGURE 14. Averaged vertical profiles of dimensionless resolvable vortex-stretching terms. Note change in abscissa scale from linear to logarithmic at ± 10.

(v) *Filtered vortex-stretching terms*

In an equation for the production of a resolvable vorticity variance, $\langle \overline{\eta}_2^2 \rangle$, where $\overline{\eta}_2$ is, for example, the component in an x–z plane, the vortex-stretching term $\langle \overline{\eta}_2^2 \partial \overline{v}/\partial y \rangle$ is believed to be a very important source (Taylor 1938). Although the present study used the primitive equations of motion rather than the set of 3 vorticity equations, it is entirely appropriate to investigate the vortex-stretching terms which may be calculated. Their averaged vertical profiles are shown in figure 14. The unexpected result is that $\langle \overline{\eta}_3^2 \partial \overline{w}/\partial z \rangle$ is negative over most of the channel. However, this result may be understood from inspection of the equation for the development of vorticity variance $\langle \overline{\eta}_3^2 \rangle$:

$$0 = \frac{\partial}{\partial t} \left\langle \frac{1}{2} \overline{\eta}_3^2 \right\rangle = -\frac{\partial}{\partial z} \left\langle \frac{1}{2} \overline{w} \overline{\eta}_3^2 \right\rangle + \left\langle \overline{\eta}_3^2 \frac{\partial \overline{w}}{\partial z} \right\rangle + \left\langle \overline{\eta}_3 \frac{\partial \overline{w}}{\partial y} \frac{\partial \overline{u}}{\partial z} \right\rangle - \left\langle \overline{\eta}_3 \frac{\partial \overline{w}}{\partial x} \frac{\partial \overline{v}}{\partial z} \right\rangle - \langle K(\nabla \overline{\eta}_3)^2 \rangle,$$

where $\overline{\eta}_3 = (\partial\overline{v}/\partial x) - (\partial\overline{u}/\partial y)$. The third term on the right is potentially large because it includes the effect of tilting by the mean shear of vorticity lying in a y–z plane, thereby converting it to vorticity in an x–y plane. It may be approximated by $\langle -(\partial\overline{u}/\partial y)(\partial\overline{w}/\partial y)\rangle\,\partial\langle\overline{u}\rangle/\partial z$ where $\partial\overline{u}/\partial y$ must be correlated with $\partial\overline{w}/\partial y$ through the correlation between $\overline{u}$ and $\overline{w}$. This term is positive because the correlation has the sign opposite from that of $\partial\langle\overline{u}\rangle/\partial z$. Thus this vortex-tilting term could more than balance the vorticity dissipation (last term), allowing the stretching term to be small and even negative except near mid channel where $\overline{u}$ and $\overline{w}$ are not correlated. No such circumstance exists in the other two vorticity equations in which the vortex-stretching terms are therefore relatively important throughout the channel.

Unfortunately, these numerical results can say nothing about the magnitude of the actual, unfiltered vortex-stretching terms in shear-flow turbulence.

10. Checks on the reliability of the numerical model

The sources of error in this numerical model are of two different kinds: those due to numerical techniques and those due to the physical assumptions. The latter consist of two types: those concerning the SGS Reynolds stresses and those concerning the boundary conditions.

(i) *Checks of numerical techniques*

Concerning the accuracy of solution of the $\nabla^2\overline{P}''$ equation, (2.7), the space-averaged normalized residual

$$\langle|\nabla^2\overline{P}'' - \partial\overline{Q}_i/\partial x_i|\rangle_V/\langle|\nabla^2\overline{P}''|\rangle_V$$

had a value of 2×10^{-4}, with the largest value at any point before space averaging being $1\cdot4\times10^{-3}$. (The angular brackets with V subscript denote the space average.) The average residual velocity divergence, also normalized, which accompanied this inaccuracy of $\nabla^2\overline{P}''$ was

$$\langle|\partial\overline{u}_i/\partial x_i|\rangle_V/\langle|\partial\overline{w}/\partial z|\rangle_V = 0\cdot5\times10^{-4},$$

with the largest value at any level without vertical averaging being $1\cdot3\times10^{-4}$. (The area-averaged, individual magnitudes of the three components of the divergence were within $\pm50\%$ of each other at all levels.) In comparison with truncation errors, these errors are very minor.

With respect to the accuracy of the finite-difference advective terms in conserving volume-averaged energy when used with the leapfrog time differencing, the following check was made. At the end of the numerical integration which has been presented, the mean shear, downstream mean pressure gradient, and eddy coefficients were all suddenly set and maintained at zero so that there were no mean energy sources or sinks. The integration then was carried 143 time steps further. There was a small increase of space-averaged energy, $E = \frac{1}{2}\langle\overline{u}_i\overline{u}_i\rangle_V$, during this period at an average dimensionless rate of $1\cdot7\times10^{-2}$. Since this rate ranges from only 1% to $0\cdot01\%$ of the rate of dissipation (see figure 8), it is safely negligible here. However, the increase was associated with forward time steps as a

jump occurred after each forward step. The magnitude of each jump was $\Delta E/E = 0.0012$. In a different test without any forward steps, but with energy sources and sinks present, an instability associated with the growth of the $2\Delta t$ oscillation occurred only after about 600 time steps. These two tests suggest, therefore, that the occasional forward step could have been performed less frequently than once each 40 time steps.

During the first of the two above checks, it was interesting to note that in only 31 time steps the resolvable shear stress $\langle \overline{uw} \rangle$ had decreased to an average of 34 % of its initial values. In the same period $\langle (\overline{u}'')^2 \rangle_V - \frac{2}{3}E$ had decreased only to 79 % of its initial value through pressure transfer to $\langle \overline{v}^2 \rangle_V$ and $\langle \overline{w}^2 \rangle_V$. Thus, isotropy for $\langle \overline{u}_i \overline{u}_j \rangle$ is approached much more rapidly when $i \neq j$.

Concerning truncation errors in the replacement of first and second spatial derivatives with centred difference formulas, no great accuracy can be claimed. The situation would not improve much by refining the grid mesh because a spectrum which decays with an exponent near $-\frac{5}{3}$ is always postulated to occur for scales near twice the grid scale. Thus there will always be considerable energy residing in scales up to 8 or 10 times the grid interval which strongly affects the resolvable velocity derivatives and which have appreciable truncation errors. An integration in three-dimensional Fourier wave space would not suffer from this difficulty, but would present a very difficult problem with respect to the boundary conditions used here near the walls.

(ii) *Checks of assumptions for the SGS Reynolds stresses*

There does not seem to be any way of comparing the eddy-coefficient representation against a better one short of additional integrations using a set of 6 differential equations for $(\partial/\partial t)\,\overline{u_i' u_j'}$, and requiring some new assumptions. However, the magnitude of K, which depends upon the constant c in (3.2), may be checked by varying c in a series of integrations. Integrations were run with $c = 0.06$, 0.08, 0.10, 0.12, 0.14 and 0.17. For the cases $0.08 \leqslant c \leqslant 0.12$ the total statistics were fairly insensitive to the particular choice of c; and for reasons already mentioned, the value $c = 0.10$ is considered about optimum.

An additional check on (3.2) would be to vary the grid volume, while holding c constant. An increase in ΔV (with small-scale averaging volume considered to increase correspondingly) may be performed after the fact. Neighbouring values of velocity may be averaged together and all finite differences may be taken across larger intervals to obtain new velocity deformations and K values. However, the statistics of the 'total' turbulence should remain invariant. This operation was performed upon the individual realizations of the ensemble of numerical results already presented. Each smoothed value of velocity was obtained from the original ones by adding $\frac{1}{8}$ the original value in with the 26 closest surrounding values, appropriately weighted. Each new grid interval was twice the original in length, so that ΔV was increased by a factor of 8. The resulting terms of the turbulence kinetic-energy budget are shown in figure 15 which is to be compared with figure 8. The mean shear was not much affected by the averaging, and the decrease of $\langle |\overline{uw}| \rangle$ which resulted was roughly compensated by the increase of $\langle |\overline{u'w'}| \rangle$ associated with the increase of K (see figure 9, dotted curve). Thus the

production term was not drastically altered by the increase of ΔV. However, for $z < 0\cdot2$, the SGS energy diffusion term is much too large, and $\langle\bar\epsilon\rangle$ is then too large as a consequence. For $z > 0\cdot25$ the SGS term is not large enough, and does not compensate for the smaller amplitudes of

$$\frac{\partial}{\partial z}\left\langle\overline{w}\,\frac{\overline{u_l''}\,\overline{u_l''}}{2}\right\rangle \quad\text{and}\quad \frac{\partial}{\partial z}\langle\overline{w}\bar{P}''\rangle.$$

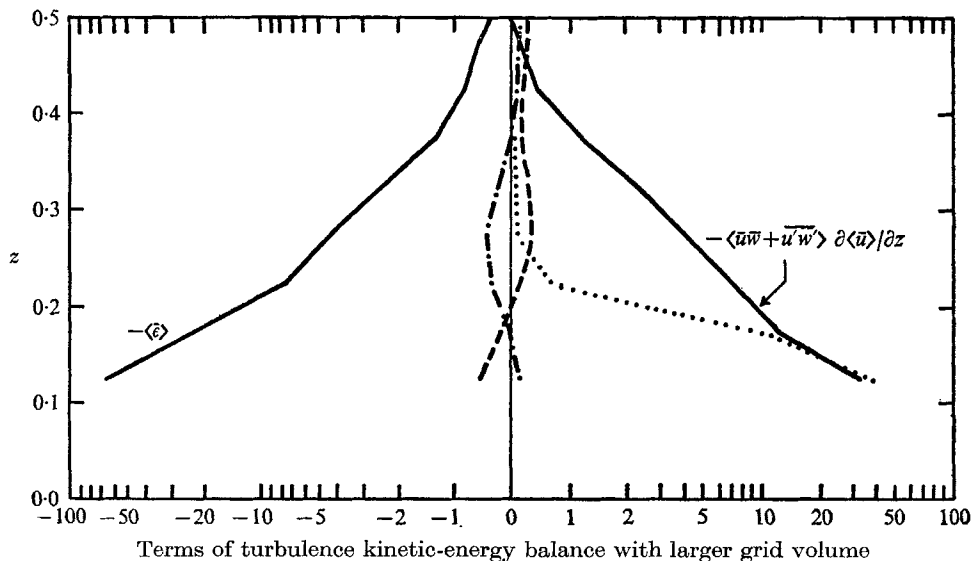Terms of turbulence kinetic-energy balance with larger grid volume

FIGURE 15. Average vertical profiles of numerically calculated terms of the turbulence kinetic-energy balance equation after the grid volume was increased eightfold. Note change in scale of abscissa from linear to logarithmic at ± 1. $-\,-\,-$, $(\partial/\partial z)\langle-\tfrac12\overline{ww}\overline{u_i''}\overline{u_i''}\rangle$; $\cdots\cdots$, $(\partial/\partial z)\langle-\overline{w'\{\tfrac12 u_i'u_i'+(p'/\rho_0 u_*^2)\}}\rangle$; $-\cdot-\cdot-$, $(\partial/\partial z)\langle-\overline{w}\bar{P}\rangle$.

Evidently, a better assumption than (9.2) is needed for the quantity

$$\frac{\partial}{\partial z}\left\langle\overline{w'\left(\frac{u_l'u_l'}{2}+\frac{p'}{\rho_0 u^{*2}}\right)}\right\rangle.$$

However, this check may be too stringent, since one would hardly consider performing a numerical integration of turbulent shear flow with only $\tfrac18$ the number of grid points used in this study.

A test on the compatibility of the K formulation with the existence of an inertial subrange would be to check for the latter in the numerical results. However, the extremely limited grid resolution did not permit the existence of any definite subrange in the numerical model.

(iii) *Checks on boundary-condition assumptions*

In placing cyclic lateral boundaries at $z = 0$, 3 and $y = 0$, $0\cdot7$, the restrictions on length and width represent assumptions. Due to computer limitations, any check performed by changing one of these limits would have to be accompanied by a change in grid resolution if the computer is employed to the same capacity.

Bearing in mind the dual nature of such a check, the upper limit of y was set at 0·5 in a preliminary integration, with Δy being decreased correspondingly. The only apparent change was a proportional decrease in the width of the elongated $\bar{u}$ eddies. For this reason, a greater y limit than that finally used would be very desirable so that more than one dominant, elongated $\bar{u}$ eddy could exist in a given horizontal plane.

Concerning boundary conditions on $\bar{u}$ and $\bar{v}$ near the walls, (6.1a, b) are quite uncertain. Different conditions which were tested at $z = \frac{1}{2}\Delta z$ are

$$\frac{\partial \bar{u}}{\partial z} = \frac{2}{\Delta z} \frac{\bar{u}}{\ln \frac{1}{2}\Delta z h/z_0}, \quad \frac{\partial \bar{v}}{\partial z} = \frac{2}{\Delta z} \frac{\bar{v}}{\ln \frac{1}{2}\Delta z h/z_0}, \qquad (10.1\,a,\,b)$$

and analogously at $z = 1 - \frac{1}{2}\Delta z$. Equation (10.1$a$) is seen to be consistent with the logarithmic law of the wall upon horizontal averaging, and both equations imply the law to hold locally also. No significant changes in the statistics were observed when (10.1a, b) were used in place of (6.1a, b). However, (6.1a, b) are preferred here in that a change of roughness length z_0 then in no way alters the details of the turbulence if the dimensionless mean flow is shifted by the same amount of all levels. With (10.1a, b), a change in z_0 does slightly affect the details of the flow.

Other checks which have been made and are reported in Deardorff (1969) concern the existence of a very small $2\Delta t$ oscillation, and the testing of boundary conditions (6.1c) and (6.3) by using alternate assumptions. In addition, the flow structure is there examined at a different time, the spatial structure of the SGS eddy coefficient is pictured, vertical profiles of velocity skewness and kurtosis are presented, longitudinal velocity spectra are examined, and assumptions are discussed further and are listed in estimated order of importance.

11. Summary and conclusions

A three-dimensional numerical model has been described for the investigation of turbulent shear flow within a channel at large Reynolds numbers. The following results, which are not amenable to easy measurements, are believed to be valid despite uncertainties arising from some of the assumptions:

(i) The longitudinal $\bar{u}$ eddies are greatly elongated downstream and resemble irregular rivers of higher speed fluid immersed in slower fluid.

(ii) The lateral $\bar{v}$ eddies have downstream tilts, but less than for the $\bar{u}$ eddies.

(iii) The $\bar{w}$ eddies show scarcely any sign of downstream tilts.

(iv) The pressure eddies are also not tilted, and frequently have maxima centred very near the walls. Their scales are slightly larger than those of the $\bar{v}$ and $\bar{w}$ eddies, and their shapes are somewhat less irregular.

(v) Helical vortices with circulations in y–z planes occur frequently and have heights ranging from half the channel height on down in scale. They are usually accompanied by relatively low pressure at their centres, and are a major source of momentum transport towards the walls.

(vi) The magnitude of the pressure fluctuations does not decrease with height as fast as the turbulence kinetic energy. The ratio of the first to the second, averaged throughout the channel, is about 0·85.

(vii) In the kinetic-energy balance equation, the pressure-diffusion term $\partial\langle\overline{w}\overline{P}''\rangle/\partial z$ has a smaller magnitude than the energy-diffusion term $\frac{1}{2}\partial\langle\overline{wu_i''u_i''}\rangle/\partial z$, and the latter is only 10% or less of the rate of dissipation throughout most of the channel.

(viii) The vortex-stretching term for *resolvable* vorticity lying in x–y planes is negative over much of the channel. For the other two vorticity components it is highly positive throughout the channel.

The following steps could be taken to improve the reliability and accuracy of the numerical model. The SGS eddy-coefficient formulation could be extended to allow anisotropy of the energy components on the sub-grid scale; or the eddy-coefficient representation could be abandoned in favour of local transport equations for the SGS Reynolds stresses; and/or the numerical resolution and size of the region treated could be increased. Although the latter two improvements would demand considerably increased dependence upon the digital computer, the rapid rate of advancement in computer technology should make them feasible in the very near future.

REFERENCES

ANGELL, J. K., PACK, D. H. & DICKINSON, C. R. 1968 *J. Atmos. Sci.* **25**, 707.

ARAKAWA, A. 1966 *J. Computational Phys.* **1**, 119.

AZIZ, K. & HELLUMS, J. D. 1967 *Phys. Fluids*, **10**, 314.

CHORIN, A. J. 1968 *Math. Computation*, **22**, 745.

COMTE-BELLOT, G. 1965 *Publ. Scientifiques et Techniques du Ministère de l'Air*, no. 419.

CORRSIN, S. 1961 *American Scientist*, **49**, 300.

DEARDORFF, J. W. 1969 *NCAR Manuscript 69–19*. Boulder, Colorado.

FISCHER, G. 1965 *Mon. Weath. Rev.* **93**, 1.

HARLOW, F. H. & WELCH, J. E. 1965 *Phys. Fluids*, **8**, 2182.

HINZE, J. O. 1959 *Turbulence*. New York: McGraw-Hill.

KASAHARA, A. & WASHINGTON, W. M. 1967 *Mon. Weath. Rev.* **95**. 7.

LAUFER, J. 1950 *NACA TN* 1053.

LAUFER, J. 1954 *NACA TR* 1174.

LEITH, C. E. 1965 *Methods in Computational Physics,* **4**. New York: Academic.

LEITH, C. E. 1968 *Proceedings of the WMO-IUGG Symposium on Numerical Weather Prediction*, Tokyo, Nov. 1968. (To be published.)

LILLY, D. K. 1967 *Proceedings of the IBM Scientific Computing Symposium on Environmental Sciences* IBM Form no. 320–1951, 195.

LUMLEY, J. L. & PANOFSKY, H. A. 1964 *Structure of Atmospheric Turbulence*. Interscience.

MINTZ, Y. 1965 *W.M.O. TN* 66, 141.

ORSZAG, S. A. 1969 *Phys. Fluids*, **12**, II–250.

REYNOLDS, O. 1895 *Phil. Trans.* A **186**, 123.

SMAGORINSKY, J., MANABE, S. & HOLLOWAY, J. L. 1965 *Mon. Weath. Rev.* **93**, 727.

TAYLOR, G. I. 1938 *Proc. Roy. Soc.* A **164**, 15.

UBEROI, M. S. 1954 *NACA TN* 3116.

UBEROI, M. S. 1963 *Phys. Fluids*, **6**, 1048.